


Phonon instability of a multi-principal element alloy

Xiao-Shi Wang and Yun-Jiang Wang ^{*}*State Key Laboratory of Nonlinear Mechanics, Institute of Mechanics, Chinese Academy of Sciences, Beijing 100190, China and School of Engineering Science, University of Chinese Academy of Sciences, Beijing 100049, China*

(Received 16 November 2022; revised 13 April 2023; accepted 9 May 2023; published 30 May 2023)

It is a common wisdom that the emergence of plasticity in crystalline solids is accompanied by the collapse of the softest vibrational mode. However, the recent advance in the multi-principal element alloys (MPEAs) complicates this scenario with essential local chemical inhomogeneity rendered by formation of the chemical short-range order (CSRO) via strong enthalpic interaction between specific atom pairs. Here we develop a set of computational metrics to characterize the features of phonons and the instability pathway in a prototypical ternary CoCrNi MPEA by atomistic simulations. There exists strong anharmonicity in MPEA quantified by a large Grüneisen parameter, which is modulated by the degree of CSRO. Both localized and extended vibrational modes exist at either low- or high-frequency vibrations, whereas extremely high-frequency modes prefer local vibration. Introduction of CSRO increases the phonon density of states at high frequency and reduces the degree of anharmonicity. Therefore, CSRO enhances elastic stability. Upon loading, phonon instability occurs via annihilation of the softest mode, akin to the scenario seen in conventional crystals. However, softening of several low-frequency modes occurs simultaneously in MPEA, and it is the cooperative softening of them that leads to the onset of plasticity. Amid phonon instability, essential variations in the Grüneisen parameter and participation ratio are observed, signifying the correlation between vibrational and configurational space in such compositional complex alloys. The results of unusual phonon features could give insight into how the structure, elasticity, and plasticity interact in generic multi-component high-entropy alloys.

DOI: [10.1103/PhysRevB.107.184116](https://doi.org/10.1103/PhysRevB.107.184116)

I. INTRODUCTION

A striking breakthrough in materials design and modulation in the last two decades is the simultaneous introduction of several multi-principal elements in one single-phase crystal, which brings about an impressive conceptional revolution in physical metallurgy termed high-entropy alloys or even high-entropy materials [1,2]. The principle of design is based on the concept of high configurational entropy with the assumption of ideal random mixing of constitute elements, which lowers the free energy and possibly yields the thermodynamically stable high-entropy materials [3–7]. This strategy does give birth to a category of unique multi-principal elemental alloys (MPEAs) with superb mechanical and functional properties, e.g., ultra strength and enhanced ductility, excellent fracture toughness and shock resistance, etc. [8–14]. The promising properties and huge design phase space of such materials motivate great interest in materials science and condensed matter physics.

The excellent mechanical properties of MPEAs as structural materials are attributed to their unique atomic-scale structures with nanometer scale chemical heterogeneity [15–17]. The uneven distribution of elements in local regions generates different atomic environments even if nominally the MPEAs are random solid solutions [18]. Recent high-resolution transmission electron microscope observations

provide compelling evidence for the existence of possible local chemical short-range order (CSRO) in a list of MPEAs [15,19–21]. The formation of CSRO is mostly driven by the strong enthalpic interaction between specific element pairs which locally dominates over the entropic contribution. Enthalpic interaction between compositions causes insufficient miscibility that controls both the occurrence and degree of CSRO far away from melting temperature [22–24]. As a result, CSRO in such alloys is strongly affected by the thermomechanical annealing process during fabrication and heat treatment. Note that CSRO is different from the long-range chemical order in intermetallics. The former produces spatial chemical heterogeneity at the nanoscale, which leads to a severe rugged potential energy landscape for plasticity carriers that is responsible for the observed sluggish diffusion [25–27] and rough pathway of dislocation motion [28–32]. All these features of the structures give rise to unusual dislocation nucleation, slip, cross slip, multiplication, and twinning plastic mechanisms rendering abnormal strength and ductility trade-off in MPEAs.

To comprehend the unprecedented mechanical properties of MPEAs, it is necessitated to probe the incipient plastic mechanism. It is common sense that the onset of plasticity should be accommodated by the phonon instability in solids [33–36]. The phonon instability criterion also sets up the ideal strength and ideal strain of a crystal [37,38]. Furthermore, the feature of the phonon is also closely associated with the thermodynamic and mechanical stability of materials [39,40]. While the phonon instability is well understood in

*yjwang@imech.ac.cn

terms of a transition from positive to imaginary vibrational frequency of the softest mode upon shear yielding, the scenario becomes intricate in MPEAs due to the appearance of complex heterogeneous local lattice structures. The spatial nature of soft modes should be significantly modified by the CSRO and, therefore, the initiation process of plasticity is not intuitive anymore. One significant question that arises is the interplay between vibration and CSRO. For example, phonon dispersion can be broadened in random alloys [41]. And both the force constant and the distribution of the phonon spectrum can be varied by the interaction between phonon and CSRO. Even in conventional elemental metals and alloys, there is a strong anharmonic effect in the elastic deformation of confined-volume materials, e.g., nanoscale pillars with a huge fraction of surface [42,43]. Anharmonicity is usually related to nonlinear elasticity due to phonon softening that is informative of plasticity in crystals. In the MPEAs, one can envisage a scenario of intrinsic lattice defects everywhere and there should be strong anharmonic effect in lattice vibrations that brings about abnormal phonon instability behaviors [44]. In other words, the chemical heterogeneity in MPEAs complicates the correlation between phonon instability and plasticity in MPEAs that deserves in-depth investigation.

To settle the issues, here we systematically survey the phonon features and the instability pathway with atomistic simulations in a CoCrNi MPEA with a varied degree of CSRO generated by combined molecular dynamics (MD)/Monte Carlo (MC) modelings. Special attention is paid to the phonon instability pathway and the spatial nature. We find strong anharmonic effect of lattice vibration in MPEAs indicated by the nontrivial Grüneisen parameter, which can be modified by the degree of CSRO. The relevance of unique phonon features upon deformation to plasticity emergence is discussed in such chemically complex concentrated alloys.

II. METHODS

A. Atomistic simulations

We fabricate the equilibrium configurations of CoCrNi MPEAs by the combined MD/MC simulations at 400 K. The tested model alloy is compositionally CoCrNi which is described by an embedded-atom method (EAM) empirical potential [22], which has been well benchmarked by either first-principles calculations or experimental data. It has been widely used to study the plastic deformation mechanism of this alloy. The samples contain $N = 6912$ atoms with 3D dimensions of $42.72 \times 42.72 \times 42.72 \text{ \AA}^3$. Periodic boundary conditions are applied for all three directions within NPT ensemble (constant number of atoms, constant pressure, and constant temperature). Temperature is controlled by the Nosé–Hoover thermostat [45]. The stress tensor is kept zero by the Parrinello–Rahman barostat.

In the unphysical MC modeling, it is allowed to swap different atoms of two species twice within ten MD steps. The MD time step for the integration of Newtonian equation is 1 fs. Sufficiently long MC iterations up to 1 000 000 cycles are carried out to get the equilibrium configurations of MPEA at 400 K. Ten samples of different degrees of CSRO are selected amid the MD/MC annealing. Hydrostatic compression and

expansion are applied on the models by quasistatic loading to derive the equation of states of these materials. Further tensile test is applied along the [001] direction to yield the samples at 300 K, from which the phonon is calculated based on Hessian matrix of strained samples after energy minimization. All the atomistic simulations herein are performed using the LAMMPS code [46]. The OVITO package is used to visualize the MPEA configurations [47].

B. Chemical order parameter

An atom-level CSRO parameter is defined as $\varphi_i = \exp(-s_i^{\text{Shannon}})$, where the Shannon entropy about a central atom is $s_i^{\text{Shannon}} = -\sum_{i=1}^n \alpha_i \ln \alpha_i$. α_i is the probability of finding one specific type of atom around the central atom in its nearest neighbors. $n = 12$ is the coordination number of the FCC lattice. The system-level order parameter φ is defined by an ensemble average of φ_i , i.e., $\varphi = \langle \varphi_i \rangle$. If the elements Co, Cr, Ni are distributed entirely randomly on the lattice site, the system-level Shannon entropy is $s_i^{\text{Shannon}} = -\sum_{i=1}^3 1/3 \ln 1/3 = 1.09$, which reaches the maximum value for this three-principal element alloy. If the atoms are not uniformly distributed in space, s_i^{Shannon} can be varied between 1.09 and 0. Then, the possible order parameter φ for any MPEA of three elements is within [1, 0.34], which correspond to a fully ordered phase and that of the random solid solution, respectively. In this context, φ is a global parameter to quantify the degree of CSRO in any crystalline material, which is easy to calculate from atomistic simulations.

C. Phonon density of states

The phonon density of states (DOS) and the polarization vector of normal mode are derived by performing diagonalization of the Hessian matrix. The total DOS is numerically estimated by binning the eigenvalues of the secular equation, i.e., $g(\omega) = \frac{1}{3N} \sum_i \delta(\omega - \omega_i)$. To further obtain the vibrational feature of a specific atom, the atomic-level partial vibrational DOS of an atom j is defined as

$$g_j(\omega) = \frac{1}{3N} \sum_i \delta(\omega - \omega_i) |\mathbf{e}_i^j|^2, \quad (1)$$

where N is the total number of atoms, ω_i represents the i th phonon frequency, and \mathbf{e}_i^j denotes the polarization vector of frequency ω_i projected to coordinate vector of the atom j . Here we employ the PHONON package implemented in LAMMPS to calculate the dynamical matrix of the system from MD simulations. The magnitude of the finite different displacement is 10^{-8} \AA in this method.

D. Grüneisen parameter

To demonstrate and quantify the degree of anharmonicity for the MPEAs, the Grüneisen parameter γ is calculated, which is directly associated to the third- and even higher-order anharmonic coefficients in the Taylor expansion of the interatomic potential energy with respect to atom displacement. First, the mode Grüneisen parameter, γ_i , is calculated by the derivative

of the phonon frequency with respect to volume variation,

$$\gamma_i = -\frac{V}{\omega_i} \left\langle \frac{\partial \omega_i}{\partial V} \right\rangle, \quad (2)$$

where V is the volume of the simulation box. The partial differential can be approximated by the numerical differentiation method [48] via

$$\gamma_i = -\frac{V}{\omega_i} \left\langle \frac{\Delta \omega_i(V)}{\Delta V} \right\rangle. \quad (3)$$

The Hessian matrix is evaluated by variation of phonon frequency at different volumes $0.995V_0$, $1.000V_0$, $1.001V_0$, respectively. V_0 is the equilibrium volume of the simulation box at 0 K. To measure the degree of anharmonicity of the MPEA system, we take the ensemble average of the mode Grüneisen parameters by $\gamma = \langle \gamma_i \rangle$. This is a global parameter to reflect the level of anharmonicity in any solid material.

E. Participation ratio of vibrational mode

To demonstrate the spatial nature of the vibrational modes in MPEA, the participation ratio is defined after the polarization vectors of all normal modes by

$$P(\omega_i) = \frac{1}{N} \frac{(\sum_j |\mathbf{e}_{i,j}|^2)^2}{\sum_j |\mathbf{e}_{i,j}|^4}, \quad (4)$$

which has been frequently employed to inform the localized or extended nature of vibration in amorphous solids [49,50]. N is the total number of atoms. $\mathbf{e}_{i,j}$ corresponds to the i th eigenvector of the normal mode for the j th atom. This formula represents the distribution of the projection length of the eigenvector values on different atoms. On the one hand, if the i th eigenvector indicates a projection on only one atom, the vibrational mode is extremely localized on a single atom and the participation ratio is equal to $1/N \approx 0$ with a huge number of atoms N in a material. If an eigenvector projects evenly on all the atoms, the participation ratio is 1 and the vibrational mode is of extended nature.

III. RESULTS AND DISCUSSION

A. CSRO and anharmonicity

Figure 1 demonstrates the strategy to fabricate atomistic CoCrNi MPEA samples with variable degrees of CSRO via MD/MC simulations at 400 K, which is an efficient temperature to perform simulated annealing of this alloy. Figure 1(a) shows the evolution of the CSRO parameter as a function of MC steps. It is notable that local chemical order is being established gradually with proceeding atom swaps by MC algorithm. There is an obvious inflection point at about the 10^4 MC step at which phase separation happens with the existence of preferred Ni-Ni and Co-Cr pairs, which has been shown in the literature [22,51,52]. The inset shows the potential energy as a function of MC steps, which indicates decreased potential energy and, consequently, more stable MPEA configuration at longer MC annealing time.

From the fragment of the annealing process, one can select a list of MPEA samples with different degrees of CSRO as demonstrated in Fig. 1(b). The ten MPEA configurations are

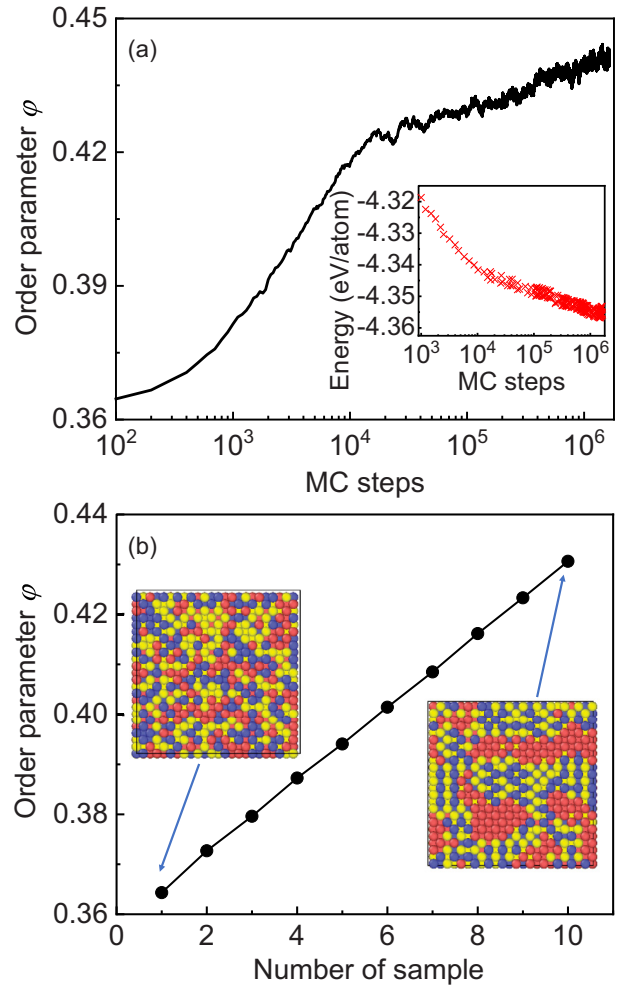


FIG. 1. Development of CSRO in CoCrNi MPEA. (a) CSRO parameter evolves with MC steps at annealing temperature 400 K. Inset: Potential energy versus MC steps. (b) Ten MPEA samples with equal intervals of CSRO. Inset: Projected plane view of the atom arrangement in the random solid solution (left upper) and the CSRO samples (right lower).

of equal intervals in linearly increasing degree of CSRO, as leveled by the magnitude of ϕ from 0.3643 to 0.4233. The inter-relationship between phonon and CSRO is probed on these samples. The two insets of Fig. 1(b) are illustrations of the MPEA samples with either random occupation or the most ordered arrangement of elements after sufficiently long-time MC annealing.

With the existence of lattice defects in crystals, or the topological disordered metals such as glasses, there are obvious anharmonic features in vibration [42,53,54]. Compared with the structural disorder materials, the chemically disordered MPEAs are still crystalline phase. However, one may anticipate some profound deviation from harmonic approximation in MPEAs since the elastic property is not uniform from region to region [55,56]. To quantitatively explore the intrinsic anharmonic feature, we plot the potential energy as a function of volumetric strain for the samples at 0 K in Fig. 2(a). Obvious asymmetry is seen in these curves regardless of the

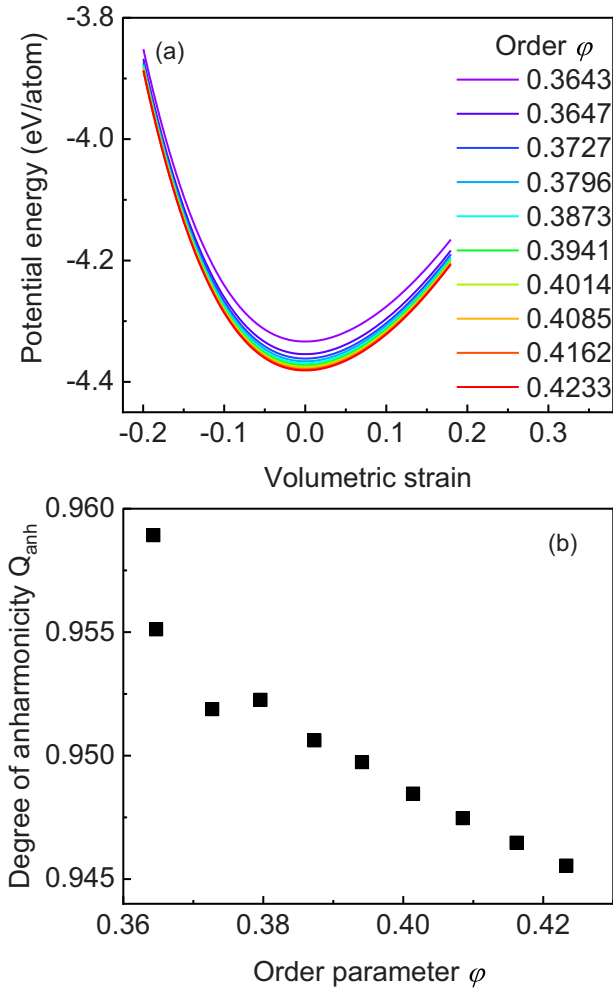


FIG. 2. Anharmonicity of the CoCrNi MPEA. (a) Potential energy versus volumetric strain of samples with different degrees of CSRO. (b) Degree of anharmonicity Q_{anh} decreases with increasing level of CSRO.

degree of CSRO in MPEAs. It means anharmonicity is an intrinsic nature of the multi-component random alloys.

To further examine how the anharmonicity is influenced by the degree of CSRO, we also expand the potential energies of MPEAs by Taylor expansion with respect to the volumetric strain. The validity of harmonic approximation is reflected by the higher order elastic constants other than the quadratic term. By this, we might define a factor to measure the Q_{anh} by simply the ratio of cubic and quadratic bulk moduli without losing too much accuracy since a cubic polynomial already produces satisfactory fits of the simulated data. In Fig. 2(b), the degree of anharmonicity Q_{anh} is plotted against the level of the chemical order ϕ . The results strongly suggest that chemical disorder brings about anharmonicity in MPEAs while chemical order drives them towards lower levels of anharmonicity. This trend could be rationalized by the feature of different atom pairs in CoCrNi MPEA. As seen in Fig. 9 in the Appendix, the Warren-Cowley parameters of Ni-Ni and Co-Cr become more negative with increasing chemical order. Therefore, the number of such like atom pairs becomes abundant in the well-annealed samples with more chemical

TABLE I. The degree of anharmonicity Q_{anh} of atomic pairs.

Pairs	Ni-Ni	Ni-Co	Ni-Cr	Co-Co	Co-Cr	Cr-Cr
Q_{anh}	0.0773	0.0799	0.0763	0.0798	0.0781	0.0804

order. Since the Ni-Ni and Co-Cr pairs are more harmonic than that of other pairs, as indicated in Table I by the degree of anharmonicity of atom pairs extracted from the empirical potentials [22], the appearance of CSRO reduces the level of anharmonicity in the studied CoCrNi MPEAs. The random solid solution with $\phi = 0.3643$ presents the strongest level of anharmonicity in these samples. One might postulate that the most ordered phase with $\phi = 1$, i.e., the long-range ordered intermetallics, may be of the most harmonic multi-component alloy.

The phonon anharmonicity can be further examined by the phonon DOS, which are calculated by direct diagonalization of the Hessian matrix of the ten annealed MPEA samples together with an absolute random solid solution. The calculated phonon DOS are displayed in Fig. 3. There are two obvious peaks in the DOS in analogy to those of the elemental FCC metals like copper and aluminum, except that the variation in DOS of MPEA is smoother, which reflects the chemical disorder characteristic. With the introduction of CSRO, the medium-frequency DOS at around 30 THz decreases, while the high-frequency modes are enhanced in the vicinity of 48 THz. The latter case is corresponding to the formation of local CSRO, which is of higher elastic modulus (rendered by stronger enthalpic interaction) that gives rise to vibrations of higher frequency. This picture points to a direction that addition of CSRO helps increase the elastic stability of the MPEA system, which should also present stronger resistance to external loadings [57]. This trend explains the recent experimentally observed strengthening of the same CoCrNi MPEA facilitated by aging sufficiently at 1000 °C [15]. Note that the position of the second peak in DOS at around 48 THz moves toward lower frequency with increasing levels of CSRO, which indicates less disorder in phonons. This is in-

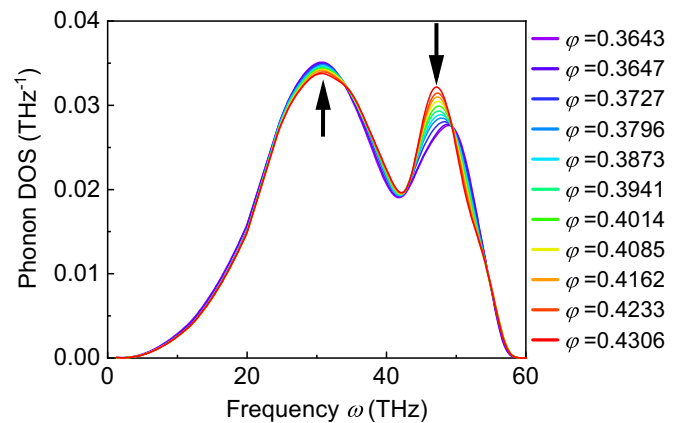


FIG. 3. Phonon density of states of MPEA samples with different levels of CSRO. The arrows indicate enhancement of the high-frequency vibrations and reduction of the medium-frequency vibrations with increasing levels of CSRO, respectively.

formed by vibrational entropy, which is calculated according to $s_{\text{vib}} = 3k_B \int_0^\infty g(\omega)[(1+n)\ln(1+n) - n\ln(n)]d\omega$. Here the Planck distribution $n(\varepsilon_i, T) = \frac{1}{e^{\beta\varepsilon_i} - 1}$, and $\varepsilon_i = \hbar\omega_i$ is phonon energy. Take 400 K, for example, the vibrational entropy of the random solid solution is $s_{\text{vib}} = 3.9665k_B$, whereas it reduces to a value of $s_{\text{vib}} = 3.9449k_B$ for the most chemically ordered sample with $\varphi = 0.4306$. Therefore, the configurational and vibrational space is correlated in MPEAs.

B. Anharmonicity informed by Grüneisen parameter

As informed by Eq. (3), the Grüneisen parameter is a dimensionless quantity measuring the variation gradient of a phonon frequency with respect to volume change. If a solid is absolutely harmonic, the shape of the curves shown in Fig. 2(a) is symmetric. In this case, the elastic constants (from curvature of energy-strain curve) remain unchanged once thermal expansion happens. Therefore, the vibrational frequency is not a function of the volume and, thus, the Grüneisen parameter $\gamma = 0$. In most of the crystals, the Grüneisen parameter is positive and lies in the range 1.5 ± 1.0 [58–60]. This means that the conventional materials are slightly anharmonic in most cases. For comparison, we calculate the Grüneisen parameters of the MPEA samples with a versatile degree of CSRO, which enables us to build a further quantitative connection between anharmonicity and the chemical order.

Both the mode Grüneisen parameters and the system-averaged counterparts are provided in Figs. 4(a) and 4(b), respectively. In Fig. 4(a), the mode Grüneisen parameters of 11 MPEA configurations are plotted as a function of the vibrational frequency. There are several features noticed from the curves. A general trend is that the mode Grüneisen parameters are positive, indicative of an anharmonic feature. Moreover, lower CSRO gives rise to a higher magnitude of mode Grüneisen parameter. This means the chemical disorder indeed induces anharmonicity in MPEAs, which is consistent with the conclusion drawn from the degree of anharmonicity in Fig. 2(b). Another striking feature is that γ_i decreases with increasing frequency. As aforementioned, the chemical disorder is a long-range feature in MPEAs, which is corresponding to the long wave-length vibrations that are more anharmonic with large Grüneisen parameters up to 5.5 in the soft modes. The critical frequency is about 15 THz, beyond which the mode Grüneisen parameter significantly levels off to a plateau below 2. This is easy to understand in terms of formation of CSRO in MPEAs. The local chemically ordered region is of higher elasticity and higher frequency, which is associated with a low degree of anharmonicity as also evidenced by decreasing Q_{anh} with φ in Fig. 2(b).

The system-level Grüneisen parameters are further shown in Fig. 4(b) as a function of the chemical order parameter φ . This system value is derived after averaging the mode Grüneisen parameters over the whole frequency domain such that it reflects globally the anharmonicity of the studied MPEAs. As expected, the higher the degree of CSRO, the smaller the system Grüneisen parameter. Introduction of the CSRO remarkably reduces the anharmonicity of the CoCrNi MPEA. Here the lowest level of anharmonicity is predicted as $\gamma = 1.45$ for the most ordered system with $\varphi = 0.4306$.

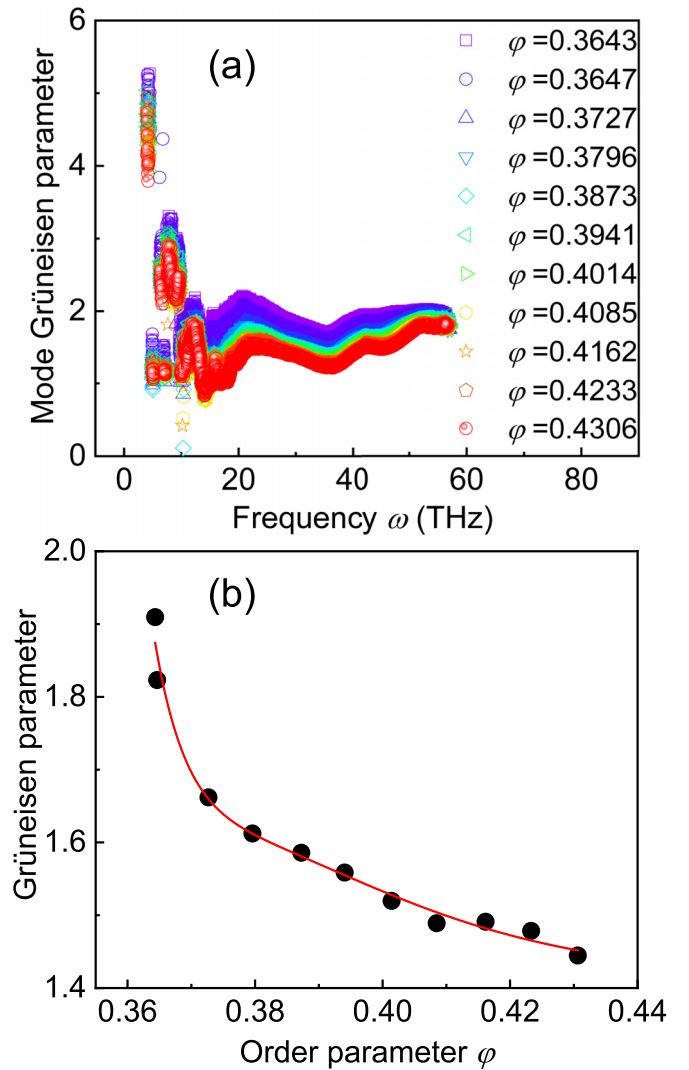


FIG. 4. Anharmonicity with Grüneisen parameter as a metric. (a) Mode Grüneisen parameter as a function of the angular frequency ω for MPEA samples with various levels of CSRO. (b) Ensemble average Grüneisen parameter as a function of CSRO. The line is a guide to the eye.

One may reasonably conjecture a scenario of an almost harmonic crystal of the same chemical compositions in the long-range ordered phases after a sufficient long time of aging at proper thermomechanical conditions. This provides an alternative solution to modulate the thermal expansion character and thermal conductivity behaviors of MPEAs through material processing without involving significant change in morphology.

C. Localized and extended modes

Checking the spatial nature of vibration is informative for the rationale of anharmonic effect and incipient plasticity in the MPEAs. Here we calculate the participation ratio $P(\omega_i)$ of each vibrational normal mode in light of Eq. (4). The mode participation ratio highly correlates with magnitude of frequency as shown in Fig. 5(a). There are three distinct regimes in the whole frequency domain. In the low-frequency regime

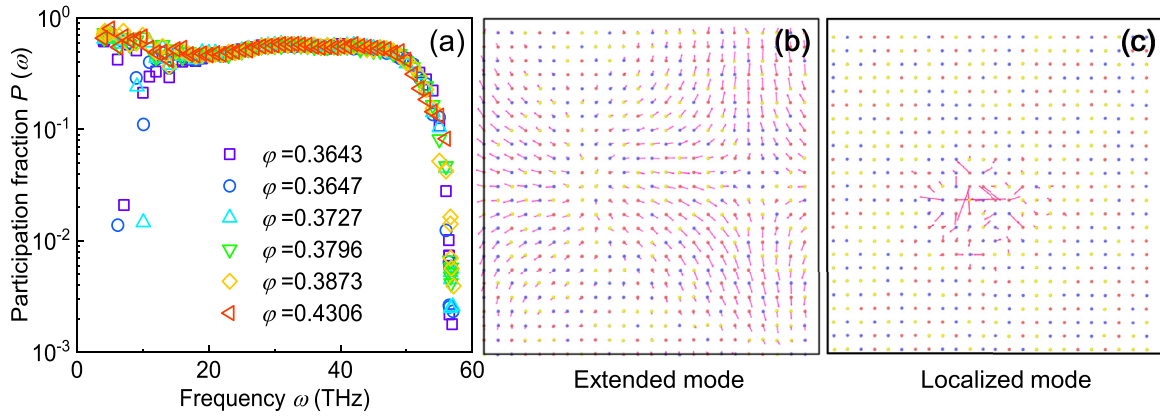


FIG. 5. Participation ratio of the vibrational modes. (a) Participation ratio as a function of mode frequency ω for samples with different level of CSRO. (b), (c) A prototypical extended mode at low frequency ($\omega = 4$ THz, $P = 0.638$) and a localized mode at high frequency ($\omega = 57$ THz, $P = 0.002$), respectively. The red arrows denote polarization vector of the vibrational mode.

below 20 THz, while the participation ratios of most normal modes are larger than 0.5, there are a few low-participation-ratio vibrations. This is not intuitive due to the fact that the low-frequency phonon of small wave number and long wavelength should involve more collective motion of a significant fraction of atoms. The soft modes with extremely high participation ratio are this kind and they are in agreement with usual knowledge. An example of an extended mode with $P = 0.638$ is demonstrated in Fig. 5(b), almost all the atoms participate in this vibration at $\omega = 4$ THz. However, the appearance of a localized vibrational mode at low frequency is a unique characteristic of the MPEA. Note that the localized low-frequency modes only exist in the disordered sample with low value of $\varphi \leq 0.3727$. One can judge that it is the chemical disorder that induces extra localized modes. This observation is in accord with broadening of the phonon dispersion line and should somehow damp the propagation of low-frequency vibration.

In the medium-frequency domain between 20 and 50 THz, there is a plateau of the participation ratio with approximately $P \sim 0.5$. This is the most frequent case that vibration involves a collective motion of a group of atoms instead of all of them, which is still an extended mode. This plateau starts to strikingly drop at a characteristic frequency $\omega = 50$ THz, which constitutes the third regime—the high-frequency localized modes. The strong vibrational mode becomes more localized at higher frequency. The participation ratio could become as small as 10^{-3} , which indicates the vibration is only contributed by a few atoms. Such a localized vibration is exemplified in Fig. 5(c) with $\omega = 57$ THz, and $P = 0.002$. Noteworthy polarization vectors are only seen in a quite limited region in the middle section of this figure. Such a localized mode at high frequency is accompanied by the formation of CSRO, which is stiffer than the rest that give birth to higher frequency vibrations. For a first approximation, the transverse sound velocity of CoCrNi $c_T \approx 2.5 \times 10^3$ m/s, which is measured experimentally by the advanced ultrasonic materials characterization system. According to $\omega = c_T q$ with $q = 2\pi/L$ being the wave number, the length scale of the high-frequency vibration with $\omega = 57$ THz is about $L = 2\pi/q = 0.28$ nm. This dimension is almost identical to the observed size of short- or medium-range chemical

order in MPEA [15,20,21]. This agreement between simulation and experiment can serve as quantitative evidence for the correspondence between the high-frequency localized mode and the sort of CSRO existing in CoCrNi MPEA.

D. Phonon instability

With the unique feature of phonons in MPEAs, one now is able to explore the onset of plastic deformation in terms of phonon instability. For this purpose, we apply tensile deformation on CoCrNi at 300 K with strain rate 10^9 s $^{-1}$ until the incipient plasticity happens at a critical strain of about $\varepsilon = 0.15$. The stress-strain curve is shown in Fig. 6(a). Then we choose a list of deformed configurations in the vicinity of yielding based on which the Hessian matrix is estimated after energy minimization. In this way, we are allowed to trace the evolution of vibrational modes during the whole process of phonon instability. In particular, the soft modes are emphasized, which are closely associated with the onset of displacive plasticity in this MPEA.

The squared vibrational frequency is proportional to the second derivative of the potential energy with respect to the coordinates at energy basin, i.e., $\omega^2 \propto \frac{\partial^2 E}{\partial R^2}$. Upon approaching the yield point, the potential surface has been flattened, which gives rise a scenario $\omega^2 = 0$. Once the energy barrier of a plastic event has been overcome, the frequency $\omega^2 < 0$. As a result, one may postulate that the yielding of this MPEA is also accommodated by the transition from positive to imaginary frequency of the soft modes. Then we choose a list of deformed configurations in the vicinity of yielding based on which the Hessian matrix is estimated after energy minimization. The characteristic frequencies obtained by Hessian matrix are ranked from smallest to largest value, that is, from soft modes to hard modes. In this way, we are allowed to trace the evolution of the vibrational modes during the whole process of phonon instability. To check the validity of the postulation, the frequencies of the first ten soft modes are shown together in light of the strain in Fig. 6(b). Before yielding, most the frequencies remain unchanged except the first four soft modes, among which the softest one fluctuates considerably in frequency up to the critical strain. Note that

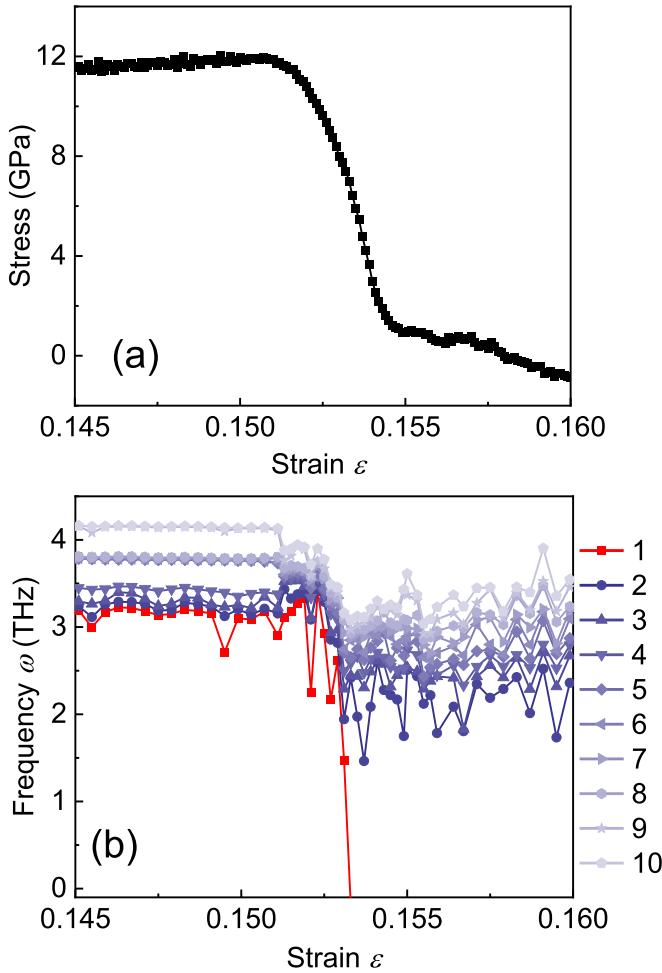


FIG. 6. Phonon instability against mechanical strain. (a) A fragment of the stress-strain curve in the vicinity of yielding. (b) Evolution of the ten softest vibrational modes versus strain. The red squared curve denotes the softest mode which loses elastic stability at strain magnitude of $\varepsilon = 0.1511$.

the elastic constant is proportional to the curvature of the local basins in the potential energy landscape. It means that both strain stiffening and strain softening occur alternatively, which are provided by the rugged potential energy landscape of two adjacent sliding planes in the complex concentrated alloy. The frequency of the softest mode becomes imaginary once $\varepsilon = 0.153$ and, therefore, this phonon loses stability. The sharp drop in frequency is in accord with the sudden strain relaxation phenomenon shown in Fig. 6(a), indicating the onset of a plastic event after releasing elastic energy. A surprising result is the simultaneous softening of all the observed soft modes once the first one collapses. This feature is different from the phonon instability of pure metals in which only collapse of the softest mode occurs [34]. This observation suggests coupling of the soft modes in MPEAs which definitely complicates the pathway of plasticity nucleation in the language of phonon instability.

To break down the complexity of the plasticity onset path, we see the failure of MPEA from different angles which include chemical order, anharmonicity as well as participation ratio, respectively, as fully illustrated by Fig. 7. First,

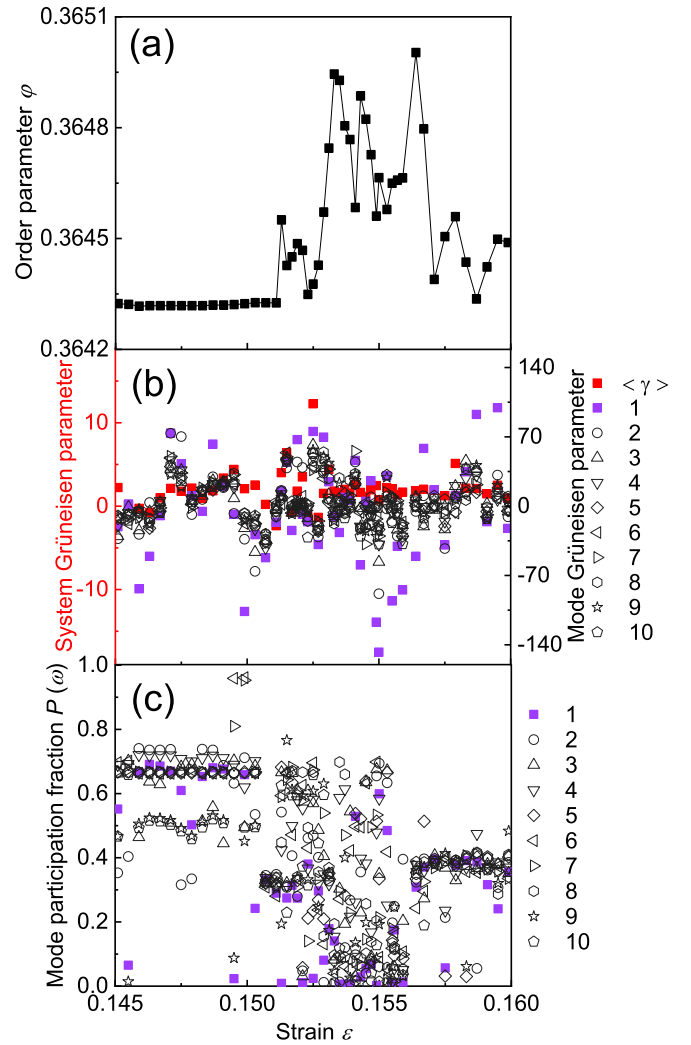


FIG. 7. Anharmonicity and participation ratio of the soft modes upon yielding. (a) Degree of CSRO as a function of strain. (b) Ensemble-average Grüneisen parameter (solid red) and those of the first ten soft vibrational modes versus strain. The Grüneisen parameter of the softest vibrational mode is signified by solid squares in purple violet. (c) Participation ratio as a function of strain for the first ten soft vibrational modes. The softest mode is emphasized by solid squares.

the plastic onset results in strong variation of the CSRO, as informed by abrupt increase of $\varphi(\varepsilon)$ upon yielding in Fig. 7(a). It is not surprising at all that structural order is broken by the nucleation of a (partial) dislocation. However, the chemical order has the opportunity to be recovered by some appropriate slip plastic mechanisms, as indicated here by the increase in φ .

In light of the anharmonic effect, the phonon instability is facilitated by huge fluctuation of the mode Grüneisen parameter of the softest vibration, as denoted by the solid squares in purple violet in Fig. 7(b). Note that there is also slight fluctuation in the system-level Grüneisen parameter (red solid), as well as those of the other nine soft modes (open symbols) except the softest one. It means that anharmonicity and its fluctuation play an important role in the phonon instability process in MPEA, especially variation in the softest mode

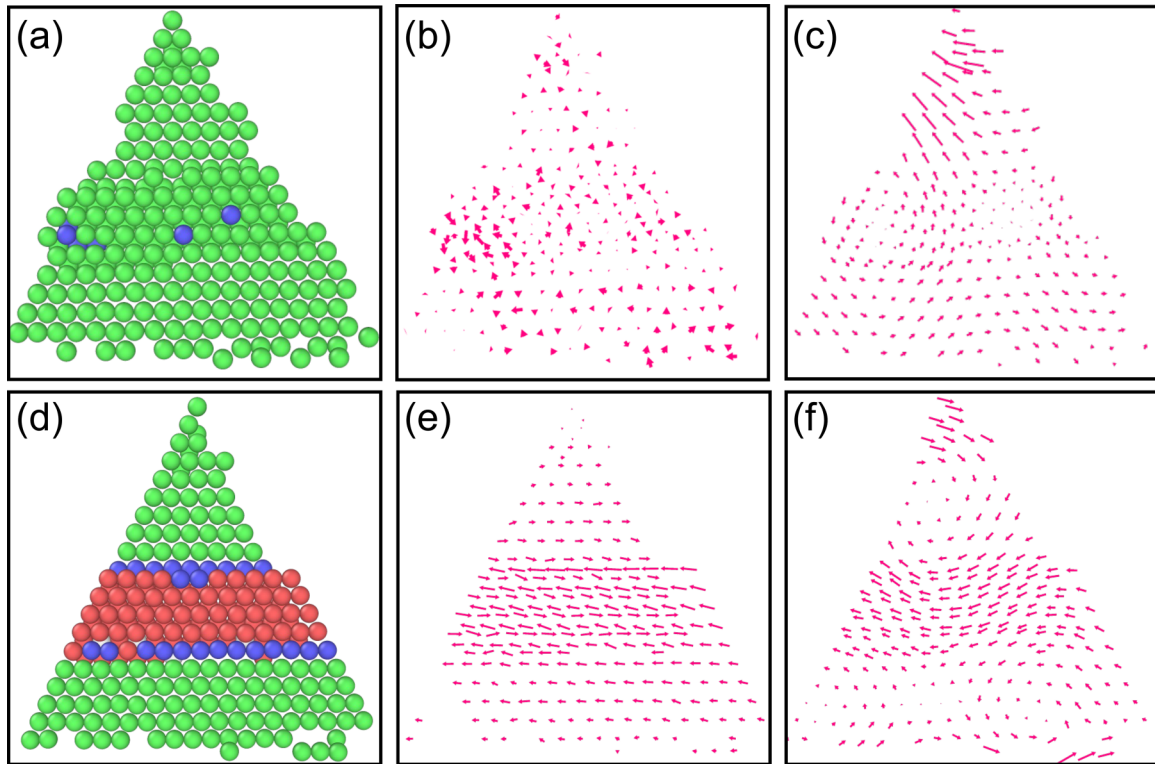


FIG. 8. Incipient plasticity informed by the spatial nature of the vibrational modes. From left to right: Atomic configurations visualized by the common neighbor analysis (CNA), the nonaffine displacement vector, and the polarization vector of the softest normal mode. (a)–(c) are for the configuration at $\varepsilon = 0.151216$ just before yielding, while (d)–(f) are for that of $\varepsilon = 0.151218$ after yielding. CNA colors: Green for FCC, blue for BCC, and red for HCP.

whose vibration polarization vector will finally transform to plastic displacement.

The participation ratio provides extra information about the spatial nature of phonon instability in MPEA. As shown in Fig. 7(c), although the participation ratios of all ten soft modes fluctuate considerably, one can still notice a clear trend of descending P_i , especially at the yielding point. Noticed from the softest mode, the participation ratio drops abruptly at the phonon instability critical point after a stable plateau. This phenomenon points to a picture of transition from an extended to localized mode in MPEA during the formation of the first plastic event. Note that the softest mode will recover to another plateau of participation ratio relatively smaller than the original value, then the mode becomes extended again, which is in agreement with the healing of chemical order shown in Fig. 7(a). In other words, the order parameter is reconstructed, anharmonicity is encouraged, and vibration becomes localized with the occurrence of phonon instability in CoCrNi MPEA, which are unique insights into the failure of chemically disordered solids that differ significantly from the usual understanding in conventional chemically homogeneous crystalline solids.

Finally, the correlation between instability of the soft mode and the emergence of the plastic event is discussed in Fig. 8. For this purpose, we show the atomic configurations and the plastic atom displacements, as well as the softest phonon polarization vector at the same moment—just before and after phonon instability, respectively. With the formation of a local stacking fault after yielding, the atoms in the middle region

undergo essential displacements that produce a partial dislocation in the sample; see the difference between nonaffine displacements shown in Figs. 8(b) and 8(e). This plastic event is actually provided by the collapse of the softest mode, as demonstrated in Figs. 8(c) and 8(f). Once the plastic event occurs, the vibrational vector rearranges to the pattern of Fig. 8(f) to accommodate the atom displacements shown in Fig. 8(e). Although the displacement field and polarization vector are not in 100% overlap, the atoms' movement directions are in basic agreement with the vibrational mode. While the displacement pattern of a dislocation is fixed in the FCC lattice, the diversity of local chemical environment renders the related soft mode frustrated in the vicinity of phonon instability.

IV. CONCLUSION

In sum, extensive atomistic simulations on a list of equilibrium CoCrNi MPEA samples provide physical insight into the phonon instability pathway in the general high-entropy alloys, with a focus on the interplay of CSRO and anharmonicity during emergence of the plastic event. The analysis of the lattice dynamics reveals a significant level of anharmonic effect in MPEA as suggested by both the equation of state and the finite value of mode- and system-level Grüneisen parameters. The anharmonicity is mostly driven by the chemical disorder, which can be reduced by the formation of CSRO in CoCrNi. There exist both extended and localized modes at low-frequency vibrations, which differs from that of conventional

pure metals in which soft modes are extended. While the existence of extra localized soft modes is accommodated by the nominally elastic heterogeneity, the high-frequency localized mode is closely related to the formation of CSRO. CSRO obviously increases the abundance of high-frequency vibrations and mildly reduces the number of the medium-frequency normal modes.

With these features in vibration of MPEA, the phonon instability mechanism is different from conventional knowledge obtained in the failure of pure metals. While phonon instability is still driven by the collapse of the softest mode, the frequency of which experiences strong fluctuations with strain. The alternative strain stiffening and softening of phonons reflect the rugged potential energy landscape of such alloys from a lattice dynamics perspective. Upon yielding, a simultaneous abrupt drop in the frequencies occurs in all ten surveyed soft modes, whereas only the first one transitions from positive to imaginary frequency. In contrast with usual knowledge, the chemical disorder brings about extra features to phonon instability in MPEAs. The chemical order can even be healed by onset of plasticity. Significant fluctuations of Grüneisen parameter (or anharmonicity) and participation ratio are clearly seen, which demonstrates the rough phonon instability pathway compared with the usual knowledge of continuous softening with strain in phonons. It is the unique order-vibration-plasticity connection in MPEAs that shifts the conventional paradigm of signifying plasticity from phonon instability.

ACKNOWLEDGMENTS

This paper was financially supported by the National Natural Science Foundation of China (Grant No. 12072344) and the Youth Innovation Promotion Association of the Chinese Academy of Sciences. The numerical calculations in this paper were carried out on the ORISE Supercomputer.

APPENDIX: WARREN-COWLEY PARAMETER VERSUS CHEMICAL ORDER

While the physical origin of the anharmonic effect in MPEAs is still an open issue, it must be associated with the variation of in chemical environment which can be leveled by the Warren-Cowley parameters $\alpha_{ij} = 1 - \frac{p_{ij}}{c_j}$ of atom pairs, where p_{ij} is the probability of finding a j -type atom around an i -type atom in the nearest neighbors. c_j is the nominal

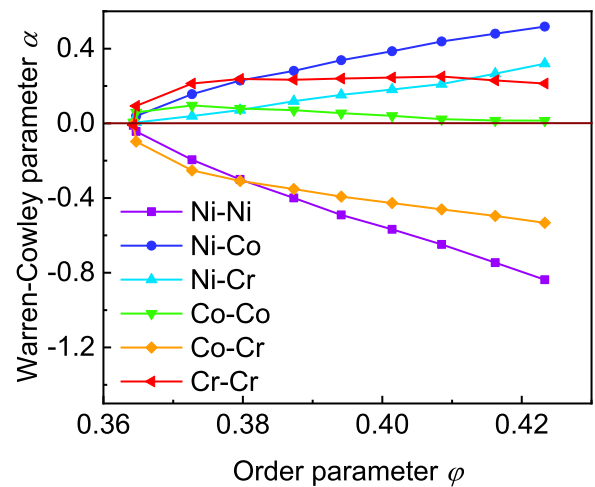


FIG. 9. Warren-Cowley parameter versus order parameter ϕ .

concentration of the j -type element in the multicomponent system. A negative value of α_{ij} indicates like pairs and a positive value implies dislike ones. The Warren-Cowley parameters are calculated and shown in Fig. 9 as a function of order parameter ϕ . The Warren-Cowley parameters of Ni-Ni and Co-Cr pairs are always negative, which means they are like atom pairs in CoCrNi alloys. The concentrations of them increase with the degree of chemical order ϕ . The Warren-Cowley parameters of Ni-Co, Ni-Cr, Co-Co, and Cr-Cr pairs are positive except the case of random solid solutions ($\phi = 0.3643$). Therefore, the four pairs are dislike pairs in the ordered configurations of CoCrNi. While the order parameter ϕ increases, $\alpha_{\text{Ni-Ni}}$ and $\alpha_{\text{Co-Cr}}$ become more negative, which indicates that the number of these two atomic pairs increases with increasing ϕ . Then the question becomes which pairs are more harmonic/anharmonic.

To answer the question, we turn the EAM potential as used here [22]. We break down the pair interactions of the empirical potential into six groups, as shown in Fig. 9. Then we expand the potential energies with Taylor expansions with respect to volume and calculate the degrees of anharmonicity Q_{anh} for different atom pairs. As shown in Table I, the degrees of anharmonicity Q_{anh} of the Ni-Ni, Ni-Cr, and Co-Cr atomic pairs are less than those of the Ni-Co, Co-Co, and Cr-Cr atomic pairs. This indicates that the anharmonic effect of the Ni-Ni and Co-Cr atomic pairs are less in CoCrNi MPEAs. As the order parameter ϕ increases, the number of Ni-Ni and Co-Cr atomic pairs increases, such that the CoCrNi MPEA becomes less anharmonic.

[1] J. W. Yeh, S. K. Chen, S. J. Lin, J. Y. Gan, T. S. Chin, T. T. Shun, C. H. Tsau, and S. Y. Chang, Nanostructured high-entropy alloys with multiple principal elements: Novel alloy design concepts and outcomes, *Adv. Eng. Mater.* **6**, 299 (2004).

[2] B. Cantor, I. Chang, P. Knight, and A. Vincent, Microstructural development in equiatomic multicomponent alloys, *Mater. Sci. Eng. A* **375-377**, 213 (2004).

[3] E. P. George, D. Raabe, and R. O. Ritchie, High-entropy alloys, *Nat. Rev. Mater.* **4**, 515 (2019).

- [4] F. Otto, Y. Yang, H. Bei, and E. George, Relative effects of enthalpy and entropy on the phase stability of equiatomic high-entropy alloys, *Acta Mater.* **61**, 2628 (2013).
- [5] Y. Zhang, Y. J. Zhou, J. P. Lin, G. L. Chen, and P. K. Liaw, Solid-solution phase formation rules for multi-component alloys, *Adv. Eng. Mater.* **10**, 534 (2008).
- [6] E. P. George and R. O. Ritchie, High-entropy materials, *MRS Bull.* **47**, 145 (2022).
- [7] Y. F. Ye, Q. Wang, J. Lu, C. T. Liu, and Y. Yang, High-entropy alloy: Challenges and prospects, *Mater. Today* **19**, 349 (2016).
- [8] Q. Ding, Y. Zhang, X. Chen, X. Fu, D. Chen, S. Chen, L. Gu, F. Wei, H. Bei, Y. Gao, M. Wen, J. Li, Z. Zhang, T. Zhu, R. O. Ritchie, and Q. Yu, Tuning element distribution, structure and properties by composition in high-entropy alloys, *Nature (London)* **574**, 223 (2019).
- [9] B. Gludovatz, A. Hohenwarter, D. Catoor, E. H. Chang, E. P. George, and R. O. Ritchie, A fracture-resistant high-entropy alloy for cryogenic applications, *Science* **345**, 1153 (2014).
- [10] Z. Lei, X. Liu, Y. Wu, H. Wang, S. Jiang, S. Wang, X. Hui, Y. Wu, B. Gault, P. Kontis, D. Raabe, L. Gu, Q. Zhang, H. Chen, H. Wang, J. Liu, K. An, Q. Zeng, T. G. Nieh, and Z. Lu, Enhanced strength and ductility in a high-entropy alloy via ordered oxygen complexes, *Nature (London)* **563**, 546 (2018).
- [11] Z. Li, K. G. Pradeep, Y. Deng, D. Raabe, and C. C. Tasan, Metastable high-entropy dual-phase alloys overcome the strength–ductility trade-off, *Nature (London)* **534**, 227 (2016).
- [12] P. Shi, R. Li, Y. Li, Y. Wen, Y. Zhong, W. Ren, Z. Shen, T. Zheng, J. Peng, X. Liang, P. Hu, N. Min, Y. Zhang, Y. Ren, P. K. Liaw, D. Raabe, and Y.-D. Wang, Hierarchical crack buffering triples ductility in eutectic herringbone high-entropy alloys, *Science* **373**, 912 (2021).
- [13] W. Li, D. Xie, D. Li, Y. Zhang, Y. Gao, and P. K. Liaw, Mechanical behavior of high-entropy alloys, *Prog. Mater. Sci.* **118**, 100777 (2021).
- [14] Q. F. He, J. G. Wang, H. A. Chen, Z. Y. Ding, Z. Q. Zhou, L. H. Xiong, J. H. Luan, J. M. Pelletier, J. C. Qiao, Q. Wang, L. L. Fan, Y. Ren, Q. S. Zeng, C. T. Liu, C. W. Pao, D. J. Srolovitz, and Y. Yang, A highly distorted ultraelastic chemically complex Elinvar alloy, *Nature (London)* **602**, 251 (2022).
- [15] R. Zhang, S. Zhao, J. Ding, Y. Chong, T. Jia, C. Ophus, M. Asta, R. O. Ritchie, and A. M. Minor, Short-range order and its impact on the CrCoNi medium-entropy alloy, *Nature (London)* **581**, 283 (2020).
- [16] P. Yu, J. P. Du, S. Shinzato, F. S. Meng, and S. Ogata, Theory of history-dependent multi-layer generalized stacking fault energy—A modeling of the micro-substructure evolution kinetics in chemically ordered medium-entropy alloys, *Acta Mater.* **224**, 117504 (2022).
- [17] S. D. Wang, X. J. Liu, Z. F. Lei, D. Y. Lin, F. G. Bian, C. M. Yang, M. Y. Jiao, Q. Du, H. Wang, Y. Wu, S. H. Jiang, and Z. P. Lu, Chemical short-range ordering and its strengthening effect in refractory high-entropy alloys, *Phys. Rev. B* **103**, 104107 (2021).
- [18] J. P. Du, P. Yu, S. Shinzato, F. S. Meng, Y. Sato, Y. Li, Y. Fan, and S. Ogata, Chemical domain structure and its formation kinetics in CrCoNi medium-entropy alloy, *Acta Mater.* **240**, 118314 (2022).
- [19] F. X. Zhang, S. Zhao, K. Jin, H. Xue, G. Velisa, H. Bei, R. Huang, J. Y. P. Ko, D. C. Pagan, J. C. Neufeind, W. J. Weber, and Y. Zhang, Local Structure and Short-Range Order in a NiCoCr Solid Solution Alloy, *Phys. Rev. Lett.* **118**, 205501 (2017).
- [20] X. Chen, Q. Wang, Z. Cheng, M. Zhu, H. Zhou, P. Jiang, L. Zhou, Q. Xue, F. Yuan, J. Zhu, X. Wu, and E. Ma, Direct observation of chemical short-range order in a medium-entropy alloy, *Nature (London)* **592**, 712 (2021).
- [21] J. Wang, P. Jiang, F. Yuan, and X. Wu, Chemical medium-range order in a medium-entropy alloy, *Nat. Commun.* **13**, 1021 (2022).
- [22] Q.-J. Li, H. Sheng, and E. Ma, Strengthening in multi-principal element alloys with local-chemical-order roughened dislocation pathways, *Nat. Commun.* **10**, 3563 (2019).
- [23] E. Antillon, C. Woodward, S. Rao, B. Akdim, and T. Parthasarathy, Chemical short range order strengthening in a model FCC high entropy alloy, *Acta Mater.* **190**, 29 (2020).
- [24] S. Yin, J. Ding, M. Asta, and R. O. Ritchie, Ab initio modeling of the energy landscape for screw dislocations in body-centered cubic high-entropy alloys, *npj Comput. Mater.* **6**, 110 (2020).
- [25] K. Y. Tsai, M. H. Tsai, and J. W. Yeh, Sluggish diffusion in Co-Cr-Fe-Mn-Ni high-entropy alloys, *Acta Mater.* **61**, 4887 (2013).
- [26] Y.-Z. Wang and Y.-J. Wang, Disentangling diffusion heterogeneity in high-entropy alloys, *Acta Mater.* **224**, 117527 (2022).
- [27] Z. Fan, B. Xing, and P. Cao, Predicting path-dependent diffusion barrier spectra in vast compositional space of multi-principal element alloys via convolutional neural networks, *Acta Mater.* **237**, 118159 (2022).
- [28] F. Wang, G. H. Balbus, S. Xu, Y. Su, J. Shin, P. F. Rottmann, K. E. Knipling, J.-C. Stinville, L. H. Mills, O. N. Senkov, I. J. Beyerlein, T. M. Pollock, and D. S. Gianola, Multiplicity of dislocation pathways in a refractory multiprincipal element alloy, *Science* **370**, 95 (2020).
- [29] B. Chen, S. Li, H. Zong, X. Ding, J. Sun, and E. Ma, Unusual activated processes controlling dislocation motion in body-centered-cubic high-entropy alloys, *Proc. Natl. Acad. Sci. USA* **117**, 16199 (2020).
- [30] J. Li, Y. Chen, Q. He, X. Xu, H. Wang, C. Jiang, B. Liu, Q. Fang, Y. Liu, Y. Yang, P. K. Liaw, and C. T. Liu, Heterogeneous lattice strain strengthening in severely distorted crystalline solids, *Proc. Natl. Acad. Sci. USA* **119**, e2200607119 (2022).
- [31] S.-C. Dai, Z.-C. Xie, and Y.-J. Wang, Atomistic interpretation of extra temperature and strain-rate sensitivity of heterogeneous dislocation nucleation in a multi-principal-element alloy, *Int. J. Plast.* **149**, 103155 (2022).
- [32] X. Wang, F. Maresca, and P. Cao, The hierarchical energy landscape of screw dislocation motion in refractory high-entropy alloys, *Acta Mater.* **234**, 118022 (2022).
- [33] K. Parlinski, Z. Q. Li, and Y. Kawazoe, First-Principles Determination of the Soft Mode in Cubic ZrO₂, *Phys. Rev. Lett.* **78**, 4063 (1997).
- [34] D. M. Clatterbuck, C. R. Krenn, M. L. Cohen, and J. W. Morris, Phonon Instabilities and the Ideal Strength of Aluminum, *Phys. Rev. Lett.* **91**, 135501 (2003).
- [35] C. A. Marianetti and H. G. Yevick, Failure Mechanisms of Graphene Under Tension, *Phys. Rev. Lett.* **105**, 245502 (2010).
- [36] A. Togo, Y. Inoue, and I. Tanaka, Phonon structure of titanium under shear deformation along 1012 twinning mode, *Phys. Rev. B* **102**, 024106 (2020).
- [37] S. Ogata, J. Li, and S. Yip, Ideal pure shear strength of aluminum and copper, *Science* **298**, 807 (2002).

- [38] S. Ogata, J. Li, N. Hirosaki, Y. Shibutani, and S. Yip, Ideal shear strain of metals and ceramics, *Phys. Rev. B* **70**, 104104 (2004).
- [39] A. van de Walle and G. Ceder, The effect of lattice vibrations on substitutional alloy thermodynamics, *Rev. Mod. Phys.* **74**, 11 (2002).
- [40] B. Fultz, Vibrational thermodynamics of materials, *Prog. Mater. Sci.* **55**, 247 (2010).
- [41] F. Körmann, Y. Ikeda, B. Grabowski, and M. H. F. Sluiter, Phonon broadening in high entropy alloys, *npj Comput. Mater.* **3**, 36 (2017).
- [42] L. Y. Chen, G. Richter, J. P. Sullivan, and D. S. Gianola, Lattice Anharmonicity in Defect-Free Pd Nanowhiskers, *Phys. Rev. Lett.* **109**, 125503 (2012).
- [43] Y.-J. Wang, G.-J. J. Gao, and S. Ogata, Size-dependent transition of deformation mechanism, and nonlinear elasticity in Ni₃Al nanowires, *Appl. Phys. Lett.* **102**, 041902 (2013).
- [44] X. Li, First-principles study of the third-order elastic constants and related anharmonic properties in refractory high-entropy alloys, *Acta Mater.* **142**, 29 (2018).
- [45] S. Nosé, A molecular dynamics method for simulations in the canonical ensemble, *Mol. Phys.* **52**, 255 (1984).
- [46] S. Plimpton, Fast parallel algorithms for short-range molecular dynamics, *J. Comput. Phys.* **117**, 1 (1995).
- [47] A. Stukowski, Visualization and analysis of atomistic simulation data with OVITO—the Open Visualization Tool, *Model. Simul. Mater. Sci. Eng.* **18**, 015012 (2010).
- [48] A. Togo and I. Tanaka, First principles phonon calculations in materials science, *Scr. Mater.* **108**, 1 (2015).
- [49] J. Yang, J. Duan, Y. J. Wang, and M. Q. Jiang, Complexity of plastic instability in amorphous solids: Insights from spatiotemporal evolution of vibrational modes, *Eur. Phys. J. E* **43**, 56 (2020).
- [50] D. Richard, K. González-López, G. Kapteijns, R. Pater, T. Vaknin, E. Bouchbinder, and E. Lerner, Universality of the Nonphononic Vibrational Spectrum Across Different Classes of Computer Glasses, *Phys. Rev. Lett.* **125**, 085502 (2020).
- [51] W.-R. Jian, Z. Xie, S. Xu, Y. Su, X. Yao, and I. J. Beyerlein, Effects of lattice distortion and chemical short-range order on the mechanisms of deformation in medium entropy alloy CoCrNi, *Acta Mater.* **199**, 352 (2020).
- [52] J. Ding, Q. Yu, M. Asta, and R. O. Ritchie, Tunable stacking fault energies by tailoring local chemical order in CrCoNi medium-entropy alloys, *Proc. Natl. Acad. Sci. USA* **115**, 8919 (2018).
- [53] Z.-Y. Yang, Y.-J. Wang, and A. Zaccone, Correlation between vibrational anomalies and emergent anharmonicity of the local potential energy landscape in metallic glasses, *Phys. Rev. B* **105**, 014204 (2022).
- [54] D. S. Kim, H. L. Smith, J. L. Niedziela, C. W. Li, D. L. Abernathy, and B. Fultz, Phonon anharmonicity in silicon from 100 to 1500 K, *Phys. Rev. B* **91**, 014307 (2015).
- [55] P. A. Geslin and D. Rodney, Microelasticity model of random alloys. Part I: Mean square displacements and stresses, *J. Mech. Phys. Solids* **153**, 104479 (2021).
- [56] P. A. Geslin, A. Rida, and D. Rodney, Microelasticity model of random alloys. Part II: Displacement and stress correlations, *J. Mech. Phys. Solids* **153**, 104480 (2021).
- [57] J. Pokluda, M. Černý, M. Šob, and Y. Umeno, Ab initio calculations of mechanical properties: Methods and applications, *Prog. Mater. Sci.* **73**, 127 (2015).
- [58] K. M. Reid, X. Yu, and D. M. Leitner, Change in vibrational entropy with change in protein volume estimated with mode Grüneisen parameters, *J. Chem. Phys.* **154**, 055102 (2021).
- [59] A. van Roekeghem, J. Carrete, and N. Mingo, Anomalous thermal conductivity and suppression of negative thermal expansion in ScF₃, *Phys. Rev. B* **94**, 020303(R) (2016).
- [60] W. Huang, B. Zhao, S. Zhu, Z. He, B. Chen, L. Wu, Z. Zhen, Y. Pu, and M. Sha, Temperature behavior of thermal expansion anisotropy, Grüneisen parameters and thermal conductivity of chalcopyrite AgGa_{0.7}In_{0.3}Se₂ crystal, *J. Alloys Compd.* **688**, 173 (2016).